



Research Note

Effect of surface topology and wettability on impacting droplet dynamics at moderate Reynolds numbers

E. Ezzatneshan*, A. Fattahi, and A. Khosroabadi

Faculty of New Technologies and Aerospace Engineering, Shahid Beheshti University, Tehran, Iran.

Received 29 August 2021; received in revised form 10 August 2022; accepted 9 March 2024

KEYWORDS

Impacting droplet;
 Surface topology;
 Wettability effect;
 Multiphase Lattice Boltzmann Method (LBM);
 Allen-Cahn equation

Abstract. The present work aims to investigate the effect of surface topology and wettability on the impacting droplet dynamics at different flow conditions. A multiphase Lattice Boltzmann Method (LBM) is employed for the simulation of interfacial dynamics. Firstly, the results obtained based on the present method for some benchmark two-phase flow problems are validated. Then, three surface topologies, including a flat substrate, semicircular cavity, and semicircular bump, are considered to get insight into the physical treatment of the impacting droplet. The present study shows that although the surface topology affects the spreading and rebounding processes of the impacting droplet, the hydrophilicity plays a significant role in the final form of the liquid phase and dictates a similar treatment for all the studied topologies. Considering different sizes for the bump, it is found that the shape of the droplet deforms almost the same immediately after the impactation for all the bump sizes, and the spreading process is not affected by the wettability. However, the receding dynamics are significantly affected by the bump size and the wetting condition of the bump surface. It is found that the contact time is minimized by incrementing the bump size and hydrophobicity of the surface.

© 2024 Sharif University of Technology. All rights reserved.

1. Introduction

There are numerous applications for impacting droplet dynamics on a solid surface, e.g., coating, anti-icing, painting, and spray cooling [1]. Therefore, the study of droplet impact on substrates is an active field of research and a matter of importance from the physical and applied points of view. Droplet impact on flat surfaces has been extensively studied through

experiments and computational techniques [2–4]. Recently, Quetzeri-Santiago et al. [3] have discussed the measurement of the dynamic contact angle and the spreading diameter of impacting droplets on a flat surface. Wei and Thoraval [4] have also numerically studied the dynamics of an air-in-liquid compound drop impacting onto a flat surface. However, understanding the physics of droplet impingement on different surface topologies has recently gained significant attention due to its complex impact on hydrodynamics and astounding industrial applications [5–7]. Ezzatneshan and Khosroabadi [5] have presented the effect of textures on

*. Corresponding author.

E-mail address: e.ezzatneshan@sbu.ac.ir (E. Ezzatneshan)

To cite this article:

E. Ezzatneshan, A. Fattahi, and A. Khosroabadi “Effect of surface topology and wettability on impacting droplet dynamics at moderate Reynolds numbers”, *Scientia Iranica* (2024), 31(8), pp. 667-680

DOI: 10.24200/sci.2024.58837.5990

a flat surface on the droplet dynamics. Dalgamoni and Yong [6] elucidated the physics of droplet impact on spherical surfaces at different flow conditions. García Pérez et al. [7] employed the Lattice Boltzmann Method (LBM) approach to Investigations of water droplet impact and freezing on a cold substrate. The ability to control the dynamics of an impacting droplet by changing the surface wettability and geometry in the micro and nano scales can affect many aspects of applications. In various applications, such as increasing the efficiency of condensation heat transfer or energy harvesting by jumping droplets, geometric structures can be used for droplet manipulation to control its dynamic behavior. Many types of surface topologies have been suggested for droplet manipulation, e.g., groove types [8,9]. In this case, some experimental measurements [10–12] and numerical predictions [13–17] have been made in the literature in the past decade.

Recently, Hu et al. [18] studied water droplet impaction on ridged superhydrophobic surfaces at varied Weber numbers. They have illustrated the droplet spreading dynamics and revealed the law on the maximum axial spreading coefficient. Huang et al. [19] have adopted a three-dimensional multi-relaxation-time pseudopotential LBM to study the double droplets' impact on a wettability-patterned surface. Gu et al. [20] have also implemented an LBM to study the reduction of the contact time of a droplet impacting a superhydrophobic substrate via adding a macro-wire or a rectangular ridge. Radhakrishnan et al. [21] have presented the impact dynamics of water droplets at the laser-patterned superhydrophobic surface. They observed finger formation at the start of the spreading, and small droplets formed at the tip of fingers, which detached from the rim during the retraction. The attention of the aforementioned works has been on the study of droplet dynamics on a flat or spherical geometry in different flow conditions. However, to the best of the authors' knowledge, the effect of different surface topologies on the impacting droplet dynamics is not thoroughly considered in the literature. The aim of the present work is to represent a comparative study of the effect of surface topology on the characteristics and pattern of an impacting droplet during the spreading, bouncing, and rebounding process by a computational model based on the LBM.

The LBM is a promising numerical technique for studying complex interfacial dynamics in multiphase flows [22–24]. The implementation of this mesoscopic method is more efficient for imposing wettability properties [25], curved and complex solid walls [26–29], and additional physical properties for special fluid flow systems [20,30,31] in comparison with the conventional numerical methods based on the Navier-Stokes equations. In the present work, a multiphase LBM based on the Allen-Cahn (A-C) equation [32] is used to study

the effect of the surface topology on the impacting droplet dynamics at different wetting conditions. The shape of the surface geometry, the size of the topology, and the contact angle of the surface are considered effective parameters. Herein, the simulation of micron-sized droplet dynamics is carried out in which the effect of gravity is stated to be insignificant. In this case, inertia, capillarity, and viscous dissipation play a dominant role in the dynamics of impact.

2. Governing equations

In the present work, the LBM with A-C equation is used for the simulation of a two-phase flow system. This numerical technique contains two equations for the particle distribution functions, namely h for the prediction of the interfacial dynamics, and g for the calculation of the hydrodynamic properties of the fluid flow. The discretized form of the prior one can be written as follows [32]:

$$h_{\alpha}(x + \mathbf{e}_{\alpha}\delta t, t + \delta t) = h_{\alpha}(x, t) - \frac{h_{\alpha}(x, t) - \bar{h}_{\alpha}^{eq}(x, t)}{\tau + 0.5} + \delta t \frac{[1 - 4(\phi - \phi_0)^2]}{\xi} \omega_{\alpha} p m b e_{\alpha} \cdot \frac{\nabla \phi}{|\nabla \phi|}, \quad (1)$$

where h_{α} is the phase-field distribution function in the position x , time t , and direction α . The vector \mathbf{e}_{α} is the microscopic velocity of particles, ω_{α} is the weighting factor, δt represents the time step, τ is the relaxation time, and ξ is the interfacial thickness that is set to be 4 grid points in the present study. The order parameter ϕ is used to track the interface and $\phi_0 = 0.5 (\phi_L + \phi_H)$ indicates the location of the interface by assuming two extreme values, ϕ_L and ϕ_H , for the bulk of light and heavy fluids, respectively. The equilibrium phase-field distribution function \bar{h}_{α}^{eq} is given as:

$$\bar{h}_{\alpha}^{eq} = h_{\alpha}^{eq} - \frac{1}{2} \delta t \frac{[1 - 4(\phi - \phi_0)^2]}{\xi} \omega_{\alpha} \mathbf{e}_{\alpha} \cdot \frac{\nabla \phi}{|\nabla \phi|}, \quad (2)$$

in which, $h_{\alpha}^{eq} = \phi \Gamma_{\alpha}$, and:

$$\Gamma_{\alpha} = \omega_{\alpha} \left[1 + \frac{\mathbf{e}_{\alpha} \cdot \mathbf{u}}{c_s^2} + \frac{(\mathbf{e}_{\alpha} \cdot \mathbf{u})^2}{2c_s^4} - \frac{(\mathbf{u} \cdot \mathbf{u})}{2c_s^2} \right]. \quad (3)$$

In Eq. (3), u indicates the macroscopic velocity vector and $c = \delta x / \delta t$ is set to as a unit. Herein, a 2D lattice with nine velocity directions (D2Q9) is considered for the discretization of the domain, as shown in Figure 1. The order parameter then can be calculated as:

$$\phi = \sum_{\alpha} h_{\alpha}, \quad (4)$$

which is used to define the macroscopic density ρ based on the light fluid density, ρ_L , and heavy fluid

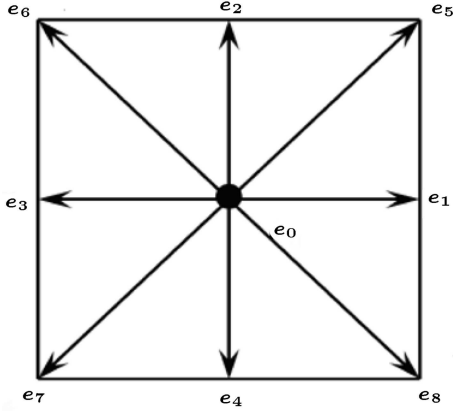


Figure 1. D2Q9 lattice model used for discretization of particle velocity in LBM.

density, ρ_H , as:

$$\rho = \rho_L + (\phi - \phi_L)(\rho_H - \rho_L). \quad (5)$$

The A-C LBM applied in the present study uses the distribution function g_α to determine the hydrodynamic properties of multiphase flow systems, including the velocity and pressure fields, as follows:

$$g_\alpha(\mathbf{x} + \mathbf{e}_\alpha \delta t, t + \delta t) = g_\alpha(\mathbf{x}, t) + \Omega_\alpha(\mathbf{x}, t) + F_\alpha(\mathbf{x}, t). \quad (6)$$

The term F_α imposes the external force F in the simulation by:

$$F_\alpha(\mathbf{x}, t) = w_\alpha \delta t \frac{\mathbf{e}_\alpha \cdot \mathbf{F}}{\rho c_s^2}. \quad (7)$$

And Ω_α describes the collision operator. Herein, to improve the numerical stability of the present A-C LBM for the simulation of multiphase flows with high-density and high-viscosity ratios, a Multiple Relaxation Time (MRT) operator is employed as follows:

$$\Omega_\alpha = -\mathbf{M}^{-1} \hat{\mathbf{S}} \mathbf{M} (g_\alpha - \bar{g}_\alpha^{eq}). \quad (8)$$

The equilibrium distribution function \bar{g}_α^{eq} is computed by:

$$\bar{g}_\alpha^{eq} = g_\alpha^{eq} - \frac{1}{2} F_\alpha, \quad (9)$$

where:

$$g_\alpha^{eq} = p^* w_\alpha + (\Gamma_\alpha - w_\alpha). \quad (10)$$

And $p^* = p/c_s^2$ is the dimensionless pressure. The orthogonal matrix \mathbf{M} transfers the distribution function from the physical space to the momentum space, and $\hat{\mathbf{S}}$ is a coefficient matrix [33]. The macroscopic pressure and velocity are then calculated as follows:

$$p^* = \sum_\alpha g_\alpha, \quad (11)$$

$$\mathbf{u} = \sum_\alpha g_\alpha \mathbf{e}_\alpha + \frac{\mathbf{F}}{2\rho} \delta t. \quad (12)$$

In the present study, the force vector \mathbf{F} is decomposed to a summation of the surface tension force \mathbf{F}_s , body force \mathbf{F}_b , pressure force \mathbf{F}_p , and viscous force \mathbf{F}_μ [5].

3. Model validation

The accuracy of the present A-C LBM for the computation of multiphase flow properties is assessed by the simulation of two test cases. The equilibrium state of a droplet on a curved surface is considered to evaluate the capability of the A-C LBM for the prediction of the contact angle imposed on the surface and the flow characteristics. Also, the spreading dynamics of an impacting droplet on a flat surface are studied to examine the accuracy of the present numerical technique for capturing the interfacial dynamics. A rectangular domain with a grid size of 200×300 is used for the simulation of the equilibrium state of the droplet on a cylinder. The diameter of the droplet and cylinder is set to be $D = 2R = 80$ and $D_c = 80$, respectively. The solutions are performed at the viscosity ratio of 100 and density ratio of 1000 with different contact angles.

The quantitative comparison of the equilibrium contact angles obtained on a cylinder surface by the present A-C LBM with those computed by the theoretical prediction based on Young’s law [5] is represented in Figure 2. It can be seen that the present results are in excellent agreement with the analytical data which confirms the accuracy and efficiency of the A-C LBM employed for resolving the morphology of the droplet in interaction with the curved solid wall for the wide range of wetting conditions. Figure 3(a)

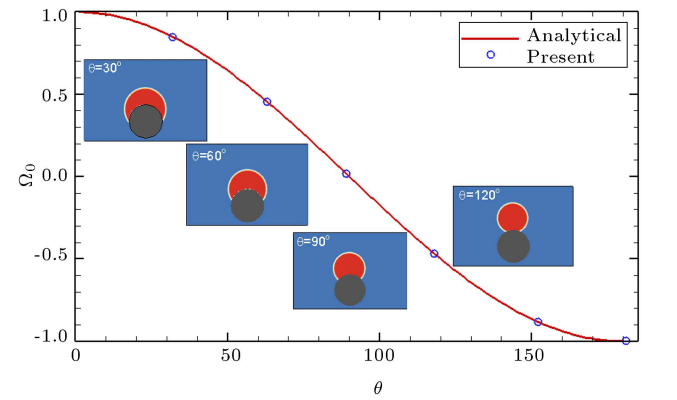


Figure 2. Results obtained by present A-C LBM for equilibrium state of a droplet on a cylinder surface at different wetting conditions, and equilibrium contact angle θ as a function of wetting potential Ω_c in comparison with analytical solution based on Young’s law.

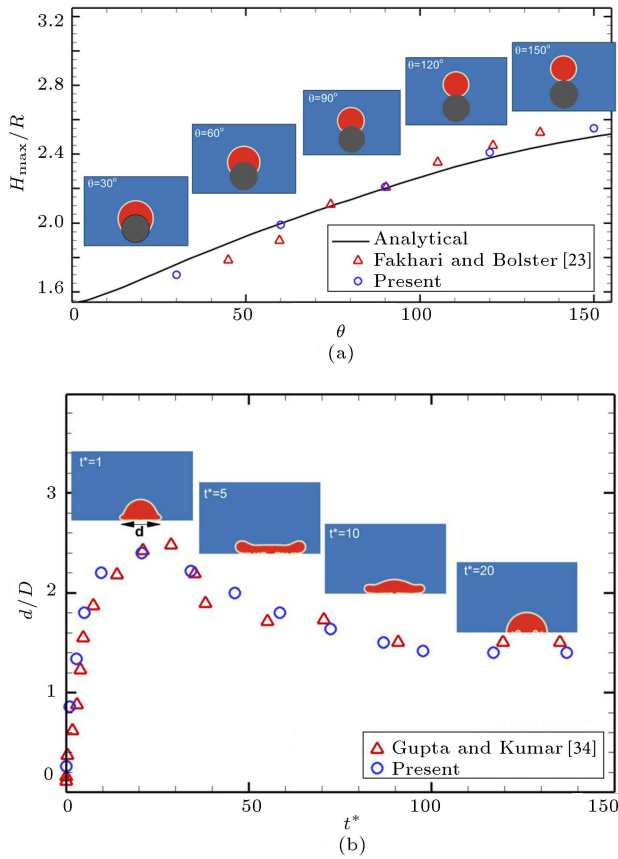


Figure 3. Comparison of present results with available data for (a) droplet equilibrium state on a cylinder at different wetting conditions and (b) instantaneous evolution of spread factor for impacting droplet on a flat surface at $Re = 30$ and $We = 40$.

demonstrates the variation of the dimensionless height of the droplet after reaching the equilibrium condition, H_{\max}/R , obtained based on the present A-C LBM in comparison with that reported in the literature [23] based on the numerical simulation and the analytical definition as:

$$\frac{H_{\max}}{R} = (1 - \cos\theta) \sqrt{\frac{\pi}{2\theta - \sin 2\theta}}. \quad (13)$$

As seen in Figure 3(a), the present results are in good agreement with the existing data that shows the A-C LBM has accurately resolved the properties of this two-phase flow system on the curved wall of the cylinder.

The dynamics of an impacting droplet on a flat surface with the contact angle $\theta = 90^\circ$ is also studied by employing a rectangular flow domain with a 200×400 mesh size at Reynolds number $Re = \frac{\rho_H u_y D}{\mu_H} = 30$ and Weber number $We = \frac{\rho_H u_y^2 D}{\sigma} = 40$. In these definitions, u_y is the vertical component of the velocity $\mathbf{u} = (0, u_y)$ that is imposed initially on the droplet and set to be $u_y = 0.005$. In this case, the instantaneous variation of the wet surface diameter d is measured, and

its dimensionless magnitude d/D is compared at the different dimensionless time $t^* = \text{iteration}/(D/u_y)$ with that obtained by Gupta and Kumar [34] in Figure 3(b). This figure indicates that the results agree well, and the present A-C LBM accurately predicts the dynamic pattern of this two-phase flow problem. The impact moment and the spreading process of the droplet on the surface are also presented in Figure 3(b) with the density field. It can be seen that some gas bubbles are trapped inside the droplet during the impaction. The good match of the results in this section with those in the literature shows that the implemented numerical technique based on the A-C LBM is capable of modeling the droplet dynamics on flat and curved surfaces with different wetting conditions at high viscosity and density ratios.

A theoretical expression supported by experimental observations is proposed by Bakshi et al. [10] for an impacting droplet onto a sphere. Herein, the A-C LBM is verified by Bakshi et al.'s work to ensure that the presented results in the present paper for the droplet dynamics on the curved topologies are accurate enough. In this test case, a droplet with the diameter $D = 60$ is initiated in the $(x_0, y_0) = (150, 450)$ inside a rectangular domain with a grid size of 300×600 . A solid circular cylinder with the radius $D_c = 60$ and contact angle of is located in the center of the computational domain at $(x_c, y_c) = (150, 300)$. Herein, the density and viscosity ratios are set to be 1000 and 100, respectively. The droplet moves towards the cylinder under the gravitational force with the Bond number of d/D :

$$Bo = \frac{g_y (\rho_H - \rho_L) D^2}{\sigma} = 2.2.$$

At the instant of impact between the droplet and the cylinder surface, when the south pole of the droplet touches the north pole of the cylinder, the time is set to be t_i , and the droplet velocity is measured as U_i . For the present test case, these values are computed as $t_i = 11250$ and $U_i = 0.0116$. Accordingly, the dimensionless time $t^* = (t - t_i) \frac{U_i}{D}$ is defined. Also, the liquid film thickness on the top of the cylinder is normalized as $h^* = h/D$. Figure 4 shows the temporal variation of h^* predicted based on the present A-C LBM in comparison with the theoretical and numerical solutions presented in the literature [10,23]. As expected from the theoretical solution, the film thickness varies as $h^* = 1 - t^*$ at the early time of the impaction. It can be seen that the present solution based on the A-C LBM is in good agreement with the theoretical and numerical solutions in this period of time. At the intermediate time, the theoretical solution proposes a power law in the form of $h^* = 0.15t^{*-2}$ for the variation of the film thickness. However, the present numerical solution, as well as the numerical

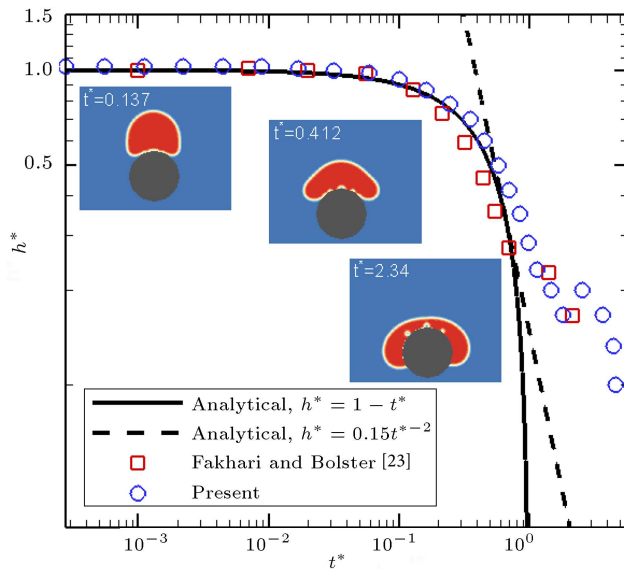


Figure 4. Comparison of instantaneous evolution of dimensionless film thickness h^* for an impacting droplet onto a cylinder obtained based on present A-C LBM with available analytical and numerical solutions at $Bo = 2.2$ and $\theta = 40^\circ$.

solution given by Fakhari and Bolster [23], show some deviation from the theoretical relation, which can be due to the unrealistic nature of 2D simulations in comparison with 3D experimental observations.

4. Results and discussions

In the present study, three surface topologies, namely the flat, cavity, and bump, are considered to investigate the effect of the geometry and wettability on the spreading dynamics of an impacting droplet on a solid wall. Figure 5 shows the topology and flow parameters of the flat, cavity, and bump geometries. Herein, the instantaneous variation of the droplet height along the centerline of the domain, H , and the arc length of the wetted surface, L , are measured during the spreading process after the impactation. A rectangular computational domain with a size of $2L_0 \times L_0$ is used for all the geometries where $L_0 = 200$. As shown in Figure 5, a droplet with the radius $R = \frac{L_0}{5}$ is placed at $x = \frac{L_0}{2}$ so that the bottom edge of the drop is tangential to the solid surface. For the cavity and bump cases, a semicircle with a radius of $R_S = 2R$ is considered as the hole and bump, respectively. The present simulations are performed at $We = 20$, $Re = 100$, and 900 and impose different wetting conditions with the contact angles of $\theta = 30^\circ, 60^\circ$, and 90° .

Figure 6 shows the results obtained based on the present A-C LBM for the impacting droplet dynamics on the flat surface. The instantaneous spreading process is demonstrated by the density contours at different contact angles. As observed in this figure, the droplet is deformed immediately after impact on

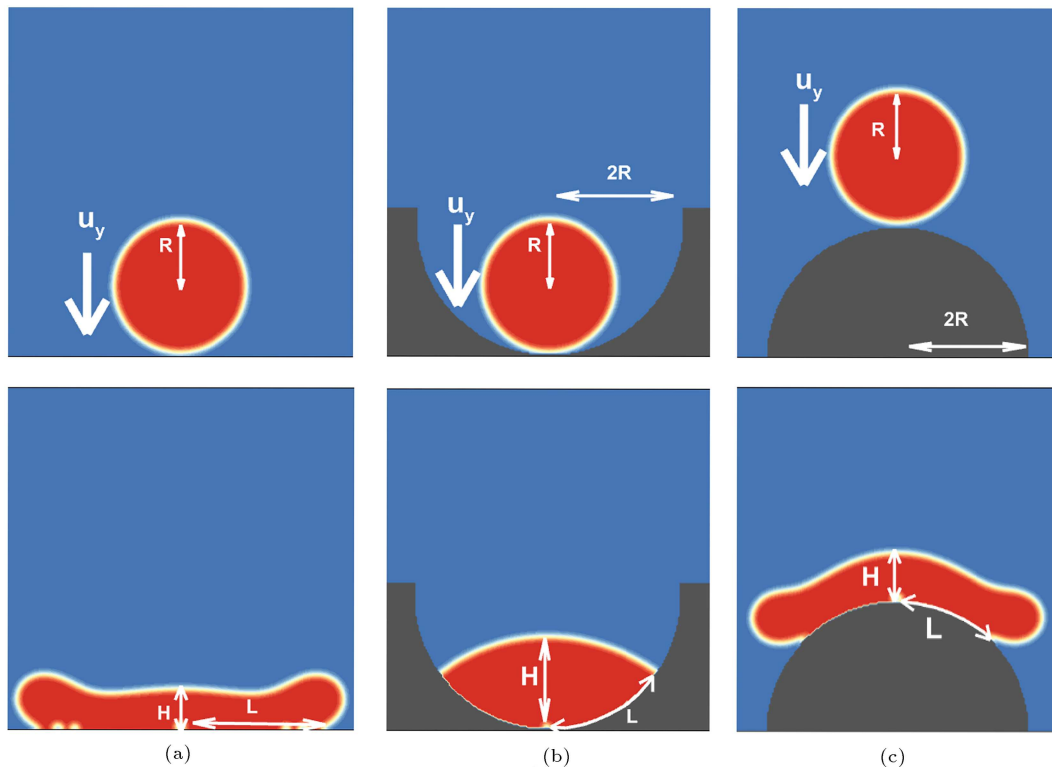


Figure 5. Surface topology and parameters used in present work for study of droplet impact on (a) Flat, (b) Cavity, and (c) Bump geometries.

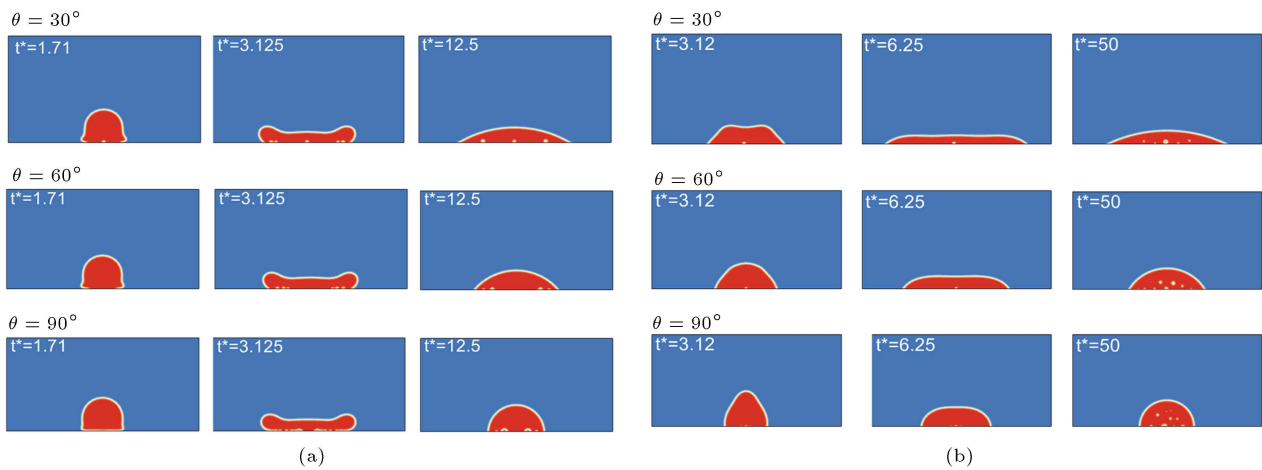


Figure 6. Instantaneous spreading process of impacting droplets on flat surface shown by density contours with $We = 20$, $\theta = 30^\circ$, 60° , and 90° at (a) $Re = 100$ and (b) $Re = 900$.

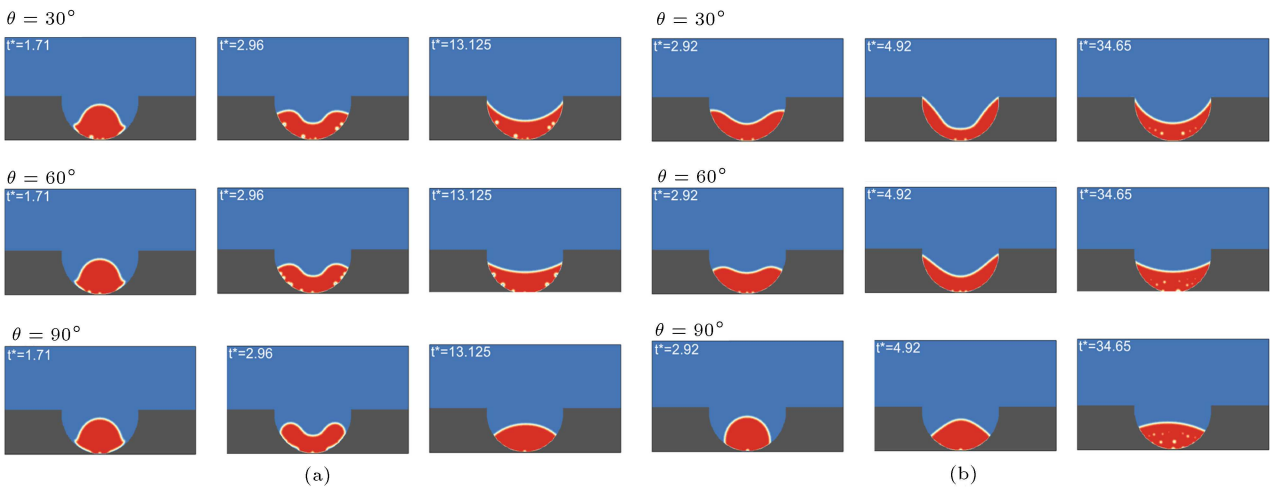


Figure 7. Instantaneous spreading process of impacting droplets in semicircle cavity shown by density contours with $We = 20$, $\theta = 30^\circ$, 60° , and 90° at (a) $Re = 100$ and (b) $Re = 900$.

the surface and a liquid lamella spreads with almost the same form for all the contact angles at $Re = 100$. However, at $Re = 900$, a significant increment in the impaction momentum affects the spreading of the liquid lamella in competition with the surface energy corresponding to the considered contact angles. Some tiny entrapped bubbles can be seen in the results presented in Figure 6, which is due to the gas phase being physically trapped between the droplet and the surface at the impaction moment [35–37]. The capture and prediction of the entrapped bubble dynamics during the spreading process, especially at the equilibrium state, demonstrate the capability of the present computational technique for studying the droplet dynamics at different flow conditions.

Figure 7 indicates the present results obtained for the impacting droplet into the cavity at the same conditions used in the previous figure. Obviously, the liquid lamella moves from the center of the cavity

along the surface and is propelled upward due to the curvature of the solid wall. In contrast with the flat surface, the cavity shape prevents the spreading droplet from forming a thin liquid layer on the solid wall. Figure 8 presents the spreading dynamics of the impacting droplet on a semicircle bump at different flow conditions considered in the present study. Similar to the flat and cavity surface topologies, this figure also shows that the form of the droplet after the impaction moment and the spreading of the liquid lamella on the bump is almost the same for all the contact angles at $Re = 100$.

The dimensionless arc length of the wetted surface, L/R , and the droplet height along the centerline of the domain, H/R , are measured to quantitatively compare the impacting droplet dynamics on the flat, cavity, and bump surfaces. Figure 9 demonstrates the comparison of these parameters for the impacting droplet at $We = 20$ and $Re = 100$ with the contact

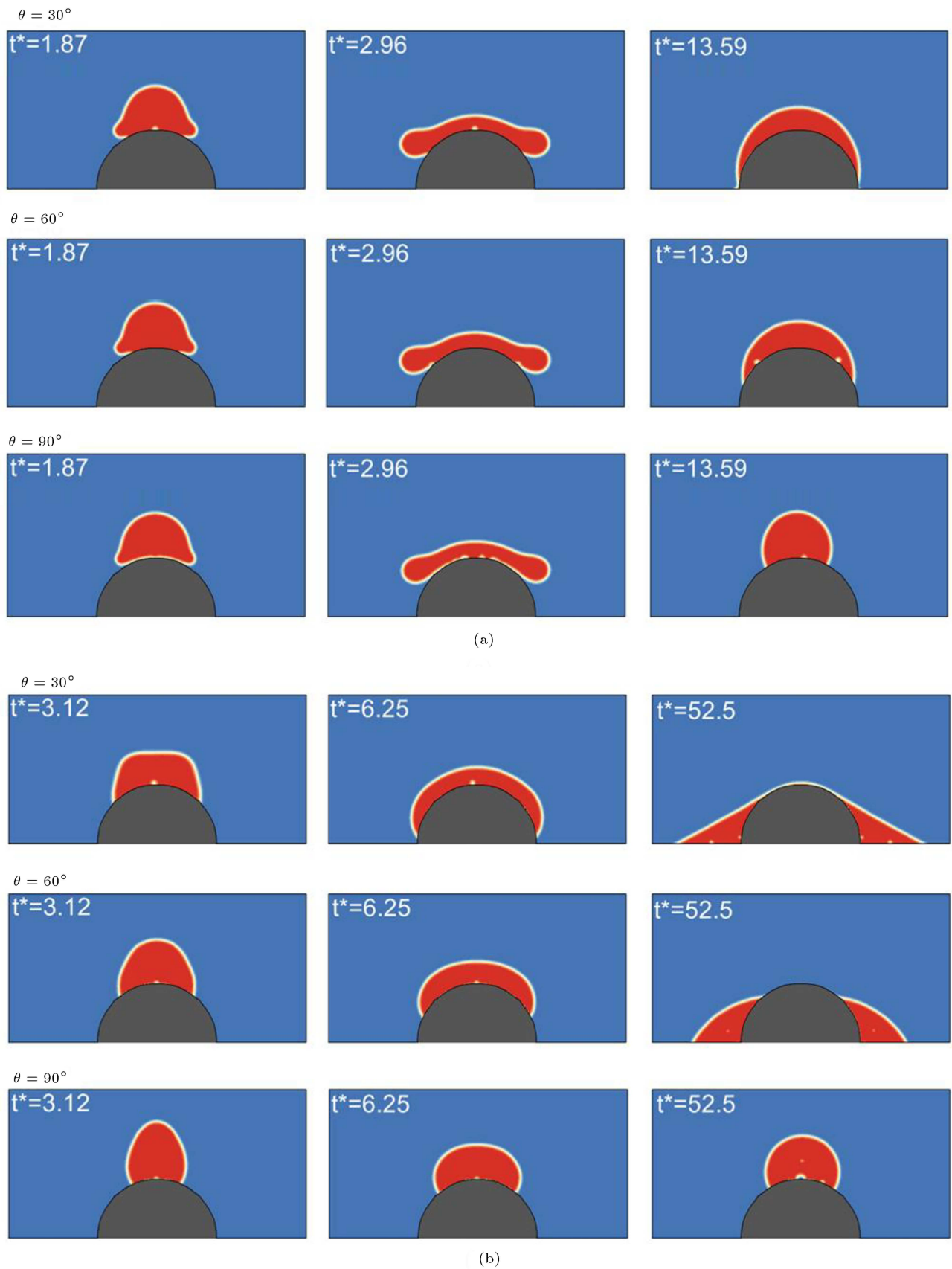


Figure 8. Instantaneous spreading process of impacting droplets on semicircle bump shown by density contours with $We = 20$, $\theta = 30^\circ$, 60° , and 90° at (a) $Re = 100$ and (b) $Re = 900$.

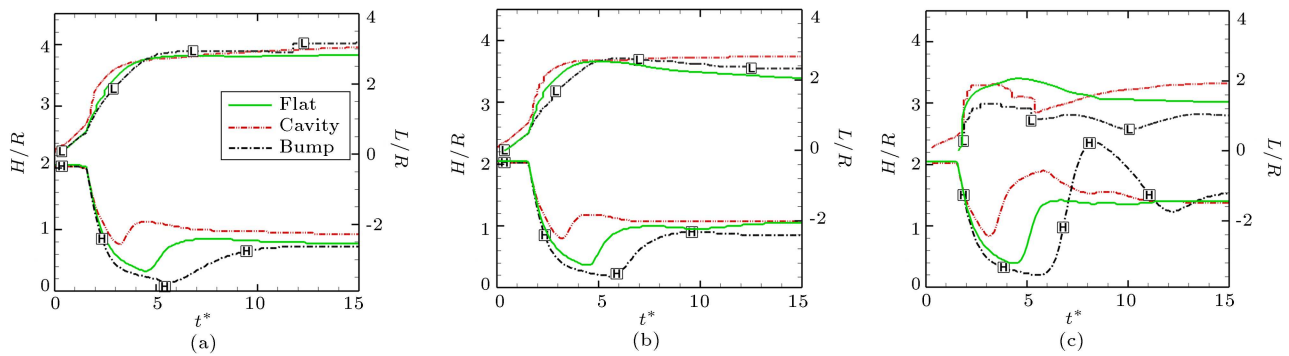


Figure 9. Comparison of dimensionless arc-length of wet area L/R (symbol L) and droplet height H/R (symbol H) during spreading process of impacting droplet on different surface topologies at $We = 20$, $Re = 100$, and (a) $\theta = 30^\circ$, (b) $\theta = 60^\circ$, (c) $\theta = 90^\circ$.

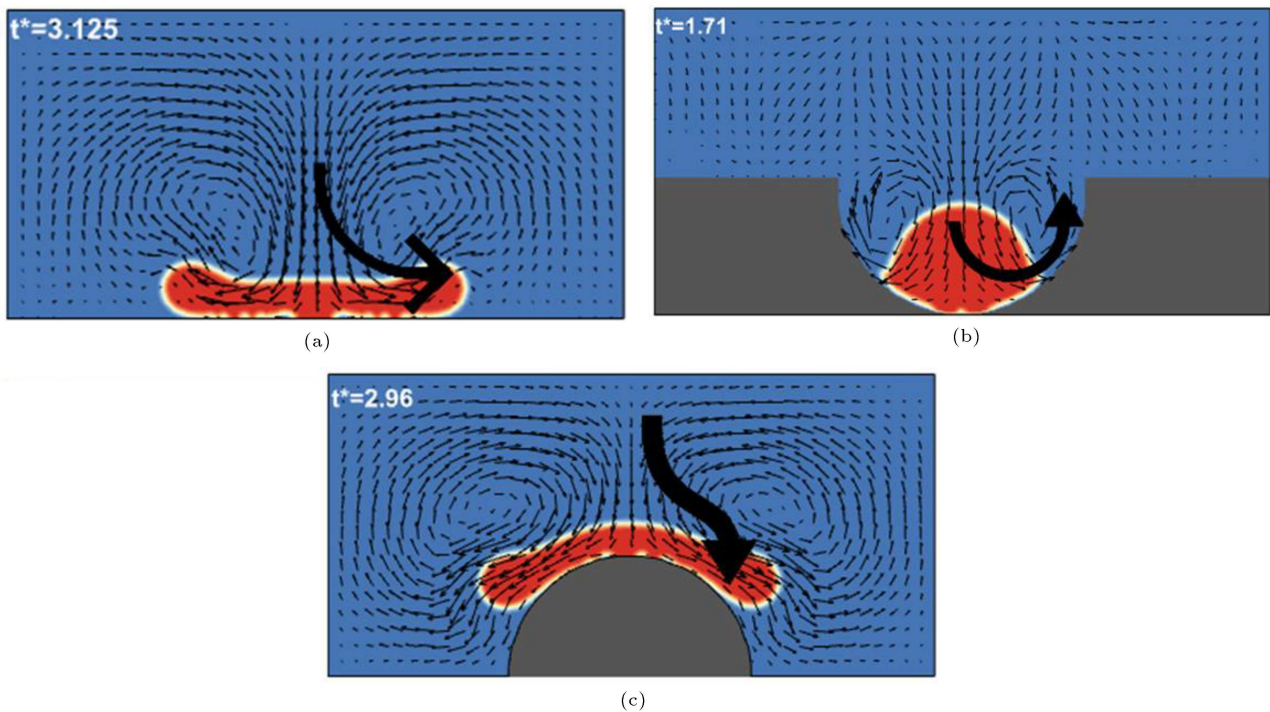


Figure 10. Velocity vectors formed during spreading process around impacting droplet at $We = 20$, $Re = 100$, and $\theta = 90^\circ$ on (a) Flat, (b) Cavity, and (c) Bump topologies.

angles of $\theta = 30^\circ$, 60° , and 90° . The results presented for H/R in this figure show that the rebounding process of the impacting droplet occurs earlier for the cavity and flat topologies, respectively, in comparison with that on the bump. Indeed, the concave shape of the cavity prevents the liquid lamella to widely spread after impact. Consequently, the interfacial tension leads to a quick rebound, and finally, a higher height for the liquid phase is measured into the cavity in comparison with the two other topologies studied. As expected, the instantiated increment of the wet area length L/R after the droplet impacts on the surface is obvious in Figure 9 for all the considered surface topologies.

In Figure 10, the mechanism of the spreading

process on the flat, cavity, and bump surfaces is demonstrated by the velocity vectors around the droplet at $We = 20$, $Re = 100$, and $\theta = 90^\circ$. As shown in this figure, the convex shape of the bump causes less deviation to the vertical impaction momentum in comparison with the flat and cavity topologies. Consequently, the droplet reaches the maximum possible spreading on the bump until the inertia of the droplet completely diminishes. However, the redirected impaction momentum due to the concave shape of the cavity surface prevents the liquid lamella from spreading, as observed on the flat and bump surfaces.

The quantitative comparison of the dimensionless arc length of the wetted surface, L/R , and the droplet

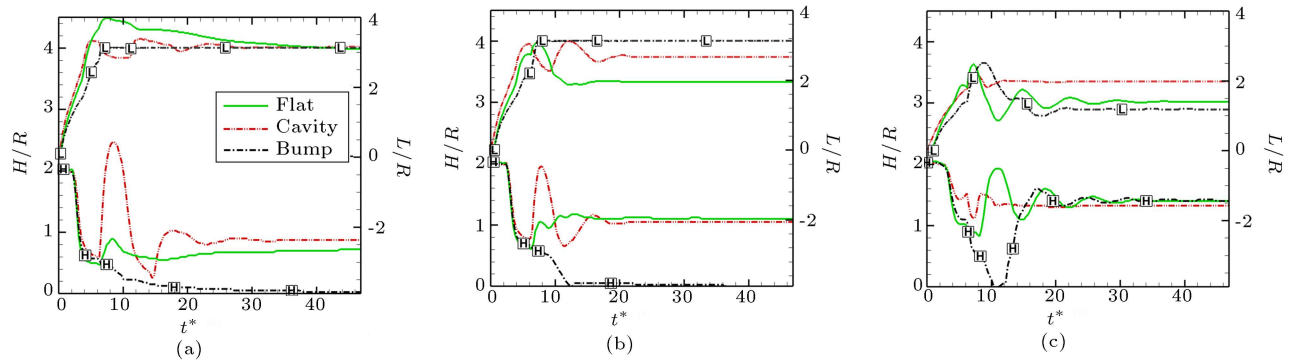


Figure 11. Comparison of dimensionless arc-length of wet area L/R (symbol L) and droplet height H/R (symbol H) during spreading process of impacting droplets on different surface topologies at $We = 20$, $Re = 900$, and (a) $\theta = 30^\circ$, (b) $\theta = 60^\circ$, and (c) $\theta = 90^\circ$.

height along the centerline of the domain, H/R , is also performed for the impacting droplet dynamics at $Re = 900$. The results obtained for the flat, cavity, and bump surfaces are presented in Figure 11. Firstly, it can be seen that the duration of the spreading process and receding of the impacting droplet are increased by the increment of the Reynolds number from $Re = 300$ to 900, regardless of the surface topology and contact angle value. Indeed, the increment of the Reynolds number causes the reduction of the viscous damping effect of the liquid against the inertial force of the impaction momentum. Therefore, the liquid lamella tends to spread widely on the surface, which leads to a higher value for L/R and a lower value for H/R at $Re = 900$ in comparison with those computed at $Re = 300$.

From Figures 9 and 11, it can be seen that at the low Reynolds number $Re = 100$, the magnitude of H/R after impaction tends to have almost the same value of $|H/R| \approx 2$ for the considered geometries. However, at the moderate Reynolds number $Re = 900$, the decrement rate of H/R is fast for more hydrophilic surfaces with $\theta = 30^\circ$ and 60° . In these cases, the final magnitude of $|H/R|$ for the bump geometry is twice its value for flat and cavity geometry. At $\theta = 90^\circ$, the variation of the $|H/R|$ value is almost the same for the three geometries. This result shows that the resistance of the surface against the droplet spreading is dominant in comparison with the surface topology. In other words, at higher contact angles, the amount of spreading can be affected by the hydrophobicity of the surface, not its geometry.

The effect of bump size on the impacting droplet dynamics is also investigated at $We = 20$ and $Re = 100$. Herein, the contact time of the droplet with the bump surface is also measured at the range of bump radius $R_S = 1.5R - 3R$ and the contact angle $\theta = 30^\circ - 120^\circ$. Figure 12 shows the sequences of droplet deformation on the bump targets during the impacting process. It can be seen that the shape of the

droplet deforms almost the same for all the considered bump sizes immediately after the impaction ($t^* = 0.15$ and 0.78). From Figure 12(a), it can be observed that the liquid lamella covers the whole surface of the small bump with radius $R_S = 1.5R$ and also spreads on the bottom wall around the bump. The hydrophilic property of the bottom wall, in this case, prevents the liquid lamella from receding. With the increment of the bump size in Figure 12(a), the spreading lamella does not contact the bottom wall around the bump and tends to recede after the spreading process. The decrement of the surface curvature with the increment of the bump size leads to a larger contact area between the liquid lamella and the surface. Therefore, after reaching the equilibrium state, the maximum height of the liquid phase has been reduced with the increment of the bump radius.

The present results in Figure 12(b) and (c) demonstrate that the impacting droplet exhibits distinct receding behavior at higher contact angles. At $\theta = 90^\circ$, despite a similar deformation process on the bump with different sizes, the droplet on the large bump reaches the equilibrium state faster than on the small bump. A completely different dynamics can be observed in Figure 12(c) for the droplet receding process on the hydrophobic bump surface at $\theta = 120^\circ$. It can be seen that the spreading is restricted immediately after impaction, and the droplet then rebounds and separates from the bump surface despite the bump size.

A similar sensitivity study is performed to investigate the effect of cavity size on the dynamics of impacting droplets at $We = 20$ and $Re = 300$. In this case, the cavity radius is set to be $R_S = 1.5R - 2.5R$, and the contact angle is considered $\theta = 30^\circ$. Figure 13 shows the sequences of droplet deformation inside the cavity during the impacting process. It can be seen that the droplet fills the cavity after impaction at $R_S = 1.5R$, and no significant dynamics are observed. However, with the increment of the cavity diameter to $R_S = 2R$

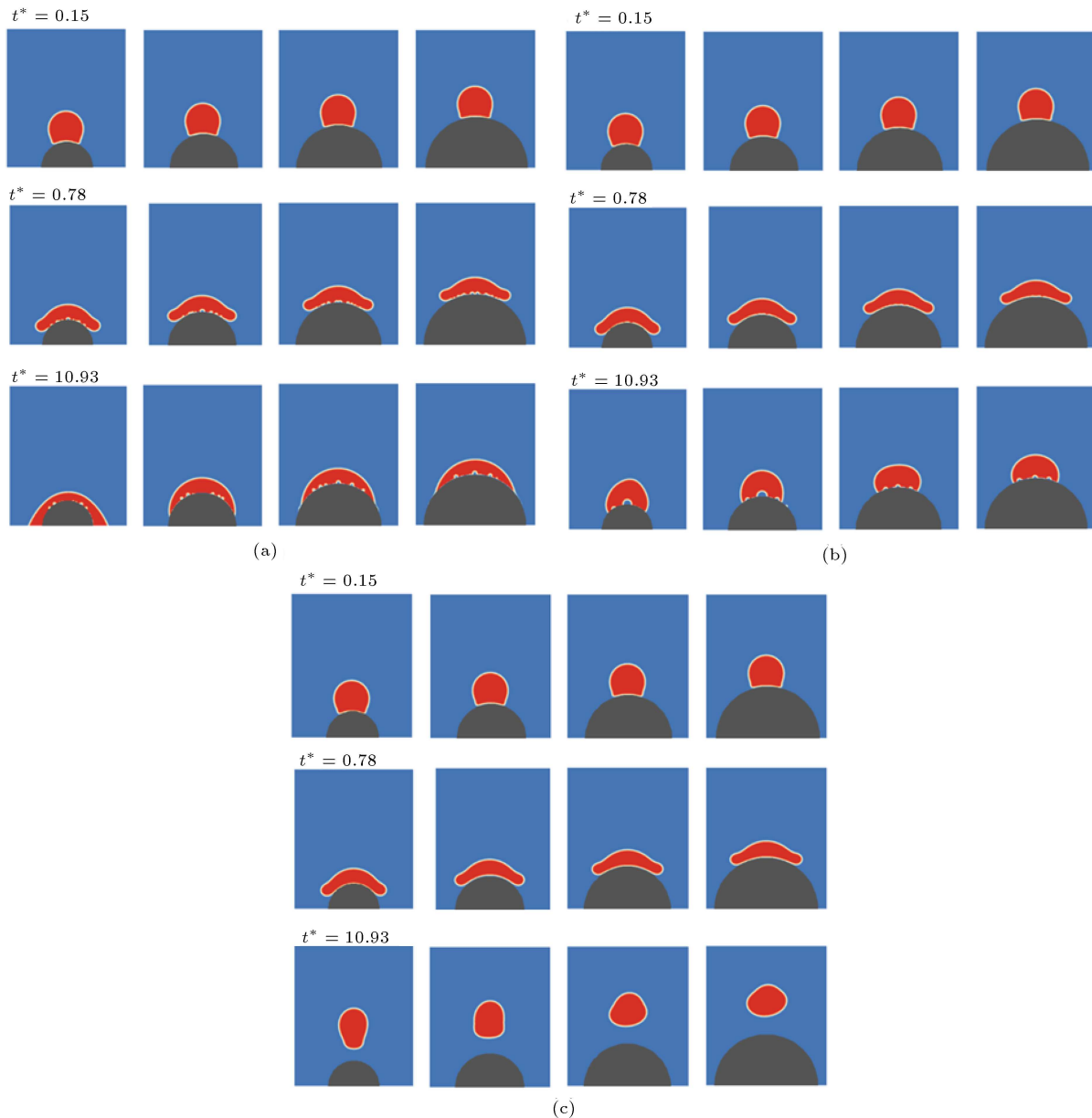


Figure 12. Instantaneous spreading process of impacting droplet on semicircle bump with radius of $1.5R$, $2R$, $2.5R$, and $3R$ (from left to right) shown by density contours with $We = 20$, $Re = 100$, at (a) $\theta = 30^\circ$, (b) $\theta = 90^\circ$ and (c) $\theta = 120^\circ$.

and $2.5R$, the impacting droplet tends to spread on the cavity surface and forms liquid lamella. Although the shape of the droplet deformation is almost the same for cavity sizes $R_S = 2R$ and $2.5R$, the increment of the cavity size leads to a larger contact area in a similar flow condition (see Figure 13(b)). Figure 13(b) demonstrates that the spreading arc length reaches a constant value faster at the cavity size $R_S = 1.5R$. However, at the period of time that arc length is almost constant for this case ($t^* > 0.7$), the droplet height exhibits oscillation, which is due to the trapping of all the liquid volume in a small hole. As the size of the cavity increases, the drop spreads more on the hydrophilic surface of the cavity (higher arc length),

and reaching the constant arc length is delayed. Due to the spreading of the liquid lamella on the cavity surface, the liquid height oscillation is not significant for the cavity sizes of $R_S = 2R$ and $2.5R$.

Additionally, the dimensionless total contact time t_{tct}^* is measured based on the present solution for the impacting droplet on the hydrophobic bump surface with $\theta = 120^\circ$ and 150° in the range of bump size $\frac{R_s}{R} = 1.5, 2, 2.5, \text{ and } 3$. Figure 14 shows the magnitude of the contact time between the droplet and the bump surface before the rebound. The reduction of the contact time with the increment of the hydrophobicity of the bump surface is obvious in this figure, which is consistent with the data reported in the literature [38,39]. Also, it was

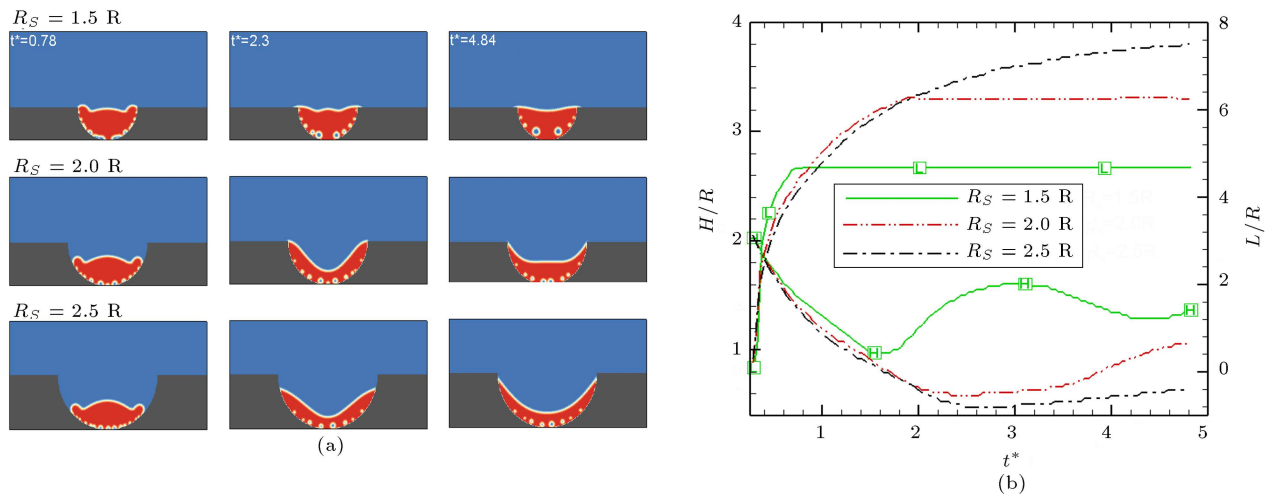


Figure 13. Instantaneous spreading process of impacting droplet in semicircle bump with radius of $1.5R$, $2R$, and $2.5R$, (a) density contours, and (b) dimensionless arc-length of wet area L/R (symbol L) and droplet height H/R (symbol H) during spreading process at $We = 20$, $Re = 300$ and $\theta = 30^\circ$.

found that bump size affects contact time in specific wettability conditions. The present results in Figure 14 demonstrate that the contact time is inversely related to the bump size so that the minimum contact time is obtained for the largest bump size considered in the present study. The reduction of the contact time is crucial in several industrial applications, e.g., to prevent ice formation on a wing by developing anti-icing surfaces in aerospace engineering. The present work indicates that the computational tool developed based on the A-C LBM is effective and accurate enough for the prediction of flow characteristics in such applications.

5. Conclusion

In the present study, the effect of the surface topology and wettability on the impacting droplet dynamics is investigated by using a computational technique based on the A-C Lattice Boltzmann Method (LBM). The model validation against the numerical and experimental data presented in the literature confirms the accuracy of the A-C LBM for the prediction of complex interfacial dynamics. The flat, semicircular cavity, and semicircular bump surface topologies are considered to study the flow pattern of the impacting droplet on different surface topologies. The present study shows that although the surface topology affects the dynamics of the impacting droplet during the spreading and rebounding processes, the hydrophilicity of the surface plays a significant role in the final form of the liquid phase and dictates a similar treatment for all the studied topologies. Also, considering different sizes for the bump, it is found that the shape of the droplet deforms almost the same immediately after the impaction for all the bump sizes, and the

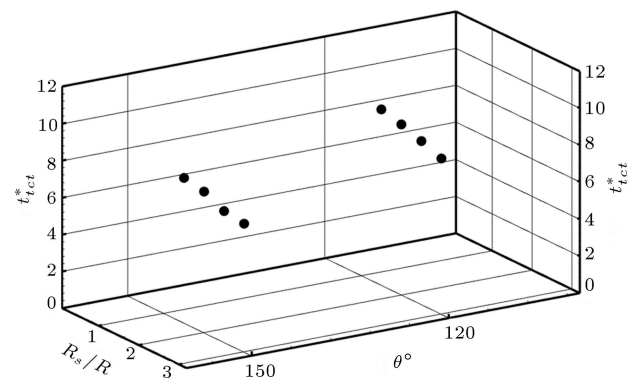


Figure 14. Total contact time computed for impacting droplets on semicircle bumps at $We=20$, $Re=100$, and contact angles of $\theta = 120^\circ$ and 150° in a range of bump size (R_s/R).

spreading process is not affected by the wettability of the surface. However, the receding dynamics are significantly affected by the bump size and the wetting condition of the bump surface. Additionally, it is found that the contact time is minimized by the increment of the bump size and the hydrophobicity of the surface.

Acknowledgment

The authors would like to thank Shahid Beheshti University for the support of this research.

Nomenclature

- C Fluid concentration
- c_s Speed of sound
- E_0 Bulk energy
- e Particle velocity

\mathbf{F}	Total force
\mathbf{F}_p	Pressure force
\mathbf{F}_b	Body force
\mathbf{F}_μ	Viscous force
\mathbf{F}_s	Surface tension force
G	Gravitational acceleration
g	Momentum distribution function
h	Concentration distribution function
M	Mobility
p	Pressure
R	Radius
t	Time
\mathbf{u}	Velocity vector
\mathbf{x}	Position
α	Lattice direction index
β	Constant parameter
Γ	Hydrodynamic equilibrium function
θ	Contact angle
κ	Coefficient related to surface tension
μ	Chemical potential
ξ	Interface thickness
ρ	Density
σ	Surface tension coefficient
τ	Relaxation time
φ	Order parameter
ω	Weighting coefficient

References

- Josserand, C. and Thoroddsen, S.T. “Drop impact on a solid surface”, *Annual Review of Fluid Mechanics*, **48**, pp. 365–391 (2016). DOI: 10.1146/annurev-fluid-122414-034401
- Breitenbach, J., Roisman, I.V., and Tropea, C. “From drop impact physics to spray cooling models: a critical review”, *Experiments in Fluids*, **59** (2018). DOI: 10.1007/s00348-018-2514-3
- Quetzeri-Santiago, M., Castrejón-Pita, A.J.R., and Castrejón-Pita, A.A. “On the analysis of the contact angle for impacting droplets using a polynomial fitting approach”, *Experiments in Fluids*, **61** (2020). DOI: 10.1007/s00348-020-02971-1
- Wei, Y. and Thoraval, M.-J. “Maximum spreading of an impacting air-in-liquid compound drop”, *Physics of Fluids*, **33**, 061703 (2021). DOI: 10.1063/5.0053384
- Ezzatneshan, E. and Khosroabadi, A. “Droplet spreading dynamics on hydrophobic textured surfaces: A Lattice Boltzmann study”, *Computers and Fluids*, 105063 (2021). DOI: 10.1016/j.compfluid.2021.105063
- Dalgamoni, H.N. and Yong, X. “Numerical and theoretical modeling of droplet impact on spherical surfaces”, *Physics of Fluids*, **33**, 052112 (2021). DOI: 10.1063/5.0047024
- García Pérez, J., Leclaire, S., Ammar, S., et al. “Investigations of water droplet impact and freezing on a cold substrate with the Lattice Boltzmann method”, *International Journal of Thermofluids*, **12**, 100109 (2021). DOI: 10.1016/j.ijft.2021.100109
- Xu, W., Lan, Z., Peng, B., et al. “Directional movement of droplets in grooves: Suspended or immersed?”, *Scientific Reports*, **6** (2016). DOI: 10.1038/srep18836
- Han, T., Noh, H., Park, H.S., et al. “Effects of wettability on droplet movement in a V-shaped groove”, *Scientific Reports*, **8** (2018). DOI: 10.1038/s41598-018-34407-6
- Bakshi, S., Roisman, I.V., and Tropea, C. “Investigations on the impact of a drop onto a small spherical target”, *Physics of Fluids*, **19**, 032102 (2007). DOI: 10.1063/1.2716065
- Charalampous, G., and Hardalupas, Y. “Collisions of droplets on spherical particles”, *Physics of Fluids*, **29**, 103305 (2017). DOI: 10.1063/1.5005124
- Banitabaei, S.A. and Amirfazli, A. “Droplet impact onto a solid sphere: Effect of wettability and impact velocity”, *Physics of Fluids*, **29**, 062111 (2017). DOI: 10.1063/1.4990088
- Mitra, S., Sathe, M.J., Doroodchi, E., et al. “Droplet impact dynamics on a spherical particle”, *Chemical Engineering Science*, **100**, pp. 105–119 (2013). DOI: 10.1016/j.ces.2013.01.037
- Zhu, Y., Liu, H.-R., Mu, K., et al. “Dynamics of drop impact onto a solid sphere: spreading and retraction”, *Journal of Fluid Mechanics*, **824** (2017). DOI: 10.1017/jfm.2017.388
- Bordbar, A., Taassob, A., Khojasteh, D., et al. “Maximum spreading and rebound of a droplet impacting onto a spherical surface at low Weber Numbers”, *Langmuir*, **34**, pp. 5149–5158 (2018). DOI: 10.1021/acs.langmuir.8b00625
- Milacic, E., Baltussen, M.W., and Kuipers, J.A.M. “Direct numerical simulation study of droplet spreading on spherical particles”, *Powder Technology*, **354**, pp. 11–18 (2019). DOI: 10.1016/j.powtec.2019.05.064
- Min, X.L. X.Z.J. “Maximum spreading of droplets impacting spherical surfaces”, *Physics of Fluids*, **31**, 092102 (2019). DOI: 10.1063/1.5117278
- Hu, Z., Zhang, X., Gao, S., et al. “Axial spreading of droplet impact on ridged superhydrophobic surfaces”, *Journal of Colloid and Interface Science*, **599**, pp. 130–139 (2021). DOI: 10.1016/j.jcis.2021.04.078

19. Huang, J., Wang, L., and He, K. “Three-dimensional study of double droplets impact on a wettability-patterned surface”, *Computers and Fluids*, **248**, 105669 (2022).
DOI: 10.1016/j.compfluid.2022.105669
20. Gu, Z., Shang, Y., Li, D., et al. “Lattice Boltzmann simulation of droplet impacting on the super hydrophobic surface with a suspended octagonal prism”, *Physics of Fluids*, **34**, 012015 (2022).
DOI: 10.1063/5.0073258
21. Radhakrishnan, J., Diaz, M., Cordovilla, F., et al. “Water droplets impact dynamics on laser engineered superhydrophobic ceramic surface”, *Optics and Laser Technology*, **158**, 108887 (2023).
DOI: 10.1016/j.optlastec.2022.108887
22. Ezzatneshan, E. “Study of surface wettability effect on cavitation inception by implementation of the lattice Boltzmann method”, *Physics of Fluids*, **29**, 113304 (2017).
DOI: 10.1063/1.4990876
23. Fakhari, A. and Bolster, D. “Diffuse interface modeling of three-phase contact line dynamics on curved boundaries: A lattice Boltzmann model for large density and viscosity ratios”, *Journal of Computational Physics*, **334**, pp. 620–638 (2017).
DOI: 10.1016/j.jcp.2017.01.025
24. Ezzatneshan, E. and Goharimehr, R. “Study of spontaneous mobility and imbibition of a liquid droplet in contact with fibrous porous media considering wettability effects”, *Physics of Fluids*, **32**, 113303 (2020).
DOI: 10.1063/5.0027960
25. Wang, X., Xu, B., Wang, Y., et al. “Directional migration of single droplet on multi-wetting gradient surface by 3D lattice Boltzmann method”, *Computers and Fluids*, **198**, 104392 (2020).
DOI: 10.1016/j.compfluid.2019.104392
26. Shen, S., Bi, F., and Guo, Y. “Simulation of droplets impact on curved surfaces with lattice Boltzmann method”, *International Journal of Heat and Mass Transfer*, **55**, pp. 6938–6943 (2012).
DOI: 10.1016/j.ijheatmasstransfer.2012.07.007
27. Ezzatneshan, E. “Implementation of D3Q19 lattice Boltzmann Method with a curved wall boundary condition for simulation of practical flow problems”, *International Journal of Engineering*, **30** (2017).
DOI: 10.5829/idosi.ije.2017.30.09c.11
28. Ezzatneshan, E. “Implementation of a curved wall and an absorbing open-boundary condition for the D3Q19 lattice Boltzmann method for simulation of incompressible fluid flows”, *Scientia Iranica*, **26**, pp. 2329–2341 (2018).
DOI: 10.24200/SCI.2018.20608
29. Ezzatneshan, E. and Goharimehr, R. “A pseudopotential lattice Boltzmann method for simulation of two-phase flow transport in porous medium at high-density and high-viscosity ratios”, *Geofluids*, **2021**, pp. 1–18 (2021).
DOI: 10.1155/2021/5668743
30. Li, Q.-Z., Lu, Z.-L., Zhou, D., et al. “Unified simplified multiphase lattice Boltzmann method for ferrofluid flows and its application”, *Physics of Fluids*, **32**, 093302 (2020).
DOI: 10.1063/5.0021463
31. Ezzatneshan, E. and Vaseghnia, H. “Dynamics of an acoustically driven cavitation bubble cluster in the vicinity of a solid surface”, *Physics of Fluids*, **33**, 123311 (2021).
DOI: 10.1063/5.0075290
32. Fakhari, A., Mitchell, T., Leonardi, C., et al. “Improved locality of the phase-field lattice-Boltzmann model for immiscible fluids at high density ratios”, *Phys Rev E*, **96**, 053301 (2017).
DOI: 10.1103/PhysRevE.96.053301
33. Lallemand, P. and Luo, L.S. “Theory of the lattice Boltzmann method: Dispersion, dissipation, isotropy, galilean invariance, and stability”, *Phys Rev E Stat Phys Plasmas Fluids Relat Interdiscip Topics*, **61**, pp. 6546–62 (2000).
DOI: 10.1103/physreve.61.6546
34. Gupta, A. and Kumar, R. “Two-dimensional lattice boltzmann model for droplet impingement and breakup in low density ratio liquids”, *Communications in Computational Physics*, **10**, pp. 767–784 (2015).
DOI: 10.4208/cicp.221209.160910a
35. Cherdantsev, A.V., Hann, D.B., Hewakandamby, H.B.N., et al. “Study of the impacts of droplets deposited from the gas core onto a gas-sheared liquid film”, *International Journal of Multiphase Flow*, **88**, pp. 69–86 (2017).
DOI: 10.1016/j.ijmultiphaseflow.2022.104033
36. Liu, Y., Tan, P., and Xu, L. “Compressible air entrapment in high-speed drop impacts on solid surfaces”, *Journal of Fluid Mechanics*, **716** (2013).
DOI: 10.1017/jfm.2012.583
37. Xiong, W. and Cheng, P. “Numerical investigation of air entrapment in a molten droplet impacting and solidifying on a cold smooth substrate by 3D lattice Boltzmann method”, *International Journal of Heat and Mass Transfer*, **124**, pp. 1262–1274 (2018).
DOI: 10.1016/j.ijheatmasstransfer.2018.04.056
38. Yarin, A.L. “Drop impact dynamics: Splashing, spreading, receding, bouncing”, *Annual Review of Fluid Mechanics*, **38**, pp. 159–192 (2006).
DOI: 10.1146/annurev.fluid.38.050304.092144
39. Antonini, C., Villa, F., Bernagozzi, I., et al. “Drop rebound after impact: The role of the receding contact angle”, *Langmuir*, **29**, pp. 16045–16050 (2013).
DOI: 10.1021/la4012372

Biographies

Eslam Ezzatneshan is a faculty member in the Aerospace Engineering Group of the Department of New Technologies Engineering at Shahid Beheshti University. He received his PhD from the Aerospace

Engineering Department at the Sharif University of Technology and did his post-doctoral research at the Chalmers University of Technology. Dr. Ezzatneshan's areas of expertise include Computational Aerodynamics and Hydrodynamics, Drag Reduction, Acoustics, and Multiphase Flows.

Ayoub Fattahi is a Senior expert in Aerospace Engineering at Shahid Beheshti University in Tehran.

He did his thesis on particulate multiphase flows. Currently, he is a designer and technical manager of Kayfiat Pooyan Co. in the pharmaceutical industry.

Aliasghar Khosroabadi is a senior expert in Aerospace Engineering at Shahid Beheshti University in Tehran. He did his thesis on multiphase flows and microfluidic systems. Currently, he is a private-sector employee in the aerospace industry.